Two-dimensional ferromagnetic van der Waals CrCl_{3} monolayer with enhanced anisotropy and Curie temperature

Feng Xue, Yusheng Hou, Zhe Wang, and Ruqian Wu

Phys. Rev. B **100**, 224429 — Published 30 December 2019

DOI: 10.1103/PhysRevB.100.224429

Two-dimensional Ferromagnetic van der Waals $CrCl_3$ Monolayer with Enhanced Anisotropy and Curie Temperature

Feng Xue[1], Yusheng Hou[2], Zhe Wang[1], Ruqian Wu[2,*]

[1] State Key Laboratory of Surface Physics and Key Laboratory for Computational Physical Sciences (MOE) and Department of Physics, Fudan University, Shanghai, 200433, China
[2] Department of Physics and Astronomy, University of California, Irvine, CA 92697-4575, USA

Abstract

Among the recently widely studied van der Waals layered magnets CrX_3 (X=Cl, Br, I), $CrCl_3$ monolayer (ML) is particularly puzzling as it is solely shown by experiments to have an in-plane magnetic easy axis and, furthermore, all of previous first-principles calculation results contradict this. Through systematical first-principles calculations, we unveil that its in-plane shape anisotropy that dominates over its weak perpendicular magnetocrystalline anisotropy is responsible for the in-plane magnetic easy axis of $CrCl_3$ ML. To tune the in-plane ferromagnetism of $CrCl_3$ ML into the desirable perpendicular one, we propose substituting Cr with isovalent tungsten (W). We find that $CrWCl_6$ has a strong perpendicular magnetic anisotropy and a high Curie temperature up to 76 K. Our work not only gives insight into understanding the two-dimensional ferromagnetism of van der Waals MLs but also sheds new light on engineering their performances for nanodevices.

Email: wur@uci.edu

I. INTRODUCTION

Ever since the discovery of grapheme [1], two-dimensional (2D) materials have attracted tremendous attention due to their unique properties and immense potential in nano device applications. Over the past decades, a variety of novel 2D materials have been successfully fabricated and extensively studied, including hexagonal boron nitride [2], silicone [3], transition metal dichalcogenides [4,5], and black phosphorous [6], to name a few. Recent discoveries of atomically thin ferromagnetic films such as $Cr_2Ge_2Te_6$ [7] and CrI_3 [8] added a new thrust in this realm as they allow integration of magnetic materials in multifunctional 2D heterostructures, essential for the design of various spintronic and topotronic devices [9-12]. Fundamentally, the long-range magnetic ordering in a 2D system is vulnerable to thermal fluctuations even at extremely low temperature, according to the Mermin-Wagner theorem [13] that was established from the isotropic Heisenberg model. A sizeable magnetic anisotropy energy which forces magnetic moments in a lattice to align in certain crystallographic direction known as easy axis becomes critical to stabilize the 2D magnetic ordering. Indeed, it was shown that the high Curie temperatures of $Cr_2Ge_2Te_6$ and CrI_3 monolayers (MLs) stem from their out-of-plane (perpendicular) magnetic anisotropy, that opens up an spin wave gap to resist the thermal agitation [7].

Chromium trihalides CrX_3 (X = Cl, Br, I) have the van der Waals layered structure and share similar physical properties. Their monolayers have been targeted as the most promising 2D magnetic materials for fundamental studies and technological innovations. Theoretical studies suggest that the magnetic easy axes of all CrX_3 monolayers are out-of-plane [14,15] just like their bulks. While recent experiments [16-21] indeed confirm this conjecture for $CrBr_3$ and CrI_3 MLs, an in-plane magnetic easy axis was observed for the $CrCl_3$ ML [17,18]. As the perpendicular easy direction of magnetic MLs is essential for the sustainability of their ferromagnetic (FM) ordering and, subsequently, for their performance in heterostructures such as inducing spin splitting on the topological surface states [22], it is important to solve the puzzle for $CrCl_3$ ML. Furthermore, it is desired to explore effective strategies to control the magnetic anisotropy and to enhance the Curie temperature (T_C) of CrX_3 MLs.

In the present work, we performed systematical first principles calculations for CrX_3 MLs and their derivations. We found that the inclusion of magnetic shape anisotropy (MSA) is crucial for studies of these thin films and is the driving force for the in-plane magnetization of the $CrCl_3$ ML. By substituting part of Cr atoms with isovalent W atoms, the magnetic easy axis of $Cr_{1-x}W_xCl_3$ MLs can be tuned to the perpendicular direction with a large magnetic anisotropy energy (MAE) of 1.07 meV per magnetic atom. Moreover, the exchange interactions among magnetic atoms are also enhanced by W substitution, resulting in a higher T_C up to 76 K. Therefore, our findings not only solve puzzles for the understanding of 2D magnetism in CrX_3 MLs, but also provide a viable strategy for optimizing their performance as needed for the development of spintronic materials and devices.

II. METHODS

The density functional theory (DFT) calculations were performed using the projector augmented wave (PAW) [23,24] method as implemented in the Vienna *ab*

initio simulation package (VASP) [25,26]. The exchange-correlation effect among electrons was described within the framework of generalized-gradient approximation (GGA), using the functional proposed by Perdew, Burke, and Ernzerhof (PBE) [27]. Note that the semi-core states of W 5*p* and Cr 3*p* were treated as valence electrons as well. For the plane wave basis expansion, we used an energy cutoff of 550 eV. We utilized a Monkhorst–Pack **k**-point mesh of 8×8×1 (4×4×1) for the CrX_3 ($Cr_{1-x}W_xCl_3$) in the structural optimization but a finer **k**-point mesh of 16×16×1 (8×8×1) in calculating the electronic and magnetic properties. The convergence with respect to **k**-point sampling was carefully tested. The vacuum space between adjacent slabs was set to be larger than 15 Å, which is enough to eliminate the spurious image interactions. Both in-plane lattice constants and atomic coordinates were fully relaxed using the conjugate gradient method until the force acting on each atom was less than 0.01 eV/Å. The electron correlation effect for the localized *d* orbitals of Cr and W atoms was treated by an effective on-site Hubbard term *U* of 3 eV.

III. RESULTS

A. Structure and magnetic properties of CrX_3

Bulk chromium trihalides have a rhombohedral structure with the $R\bar{3}$ symmetry at low temperature, and a monoclinic structure with the C2/m symmetry at high temperature. After the exfoliation, only one type of ML is found [Fig. 1(a)]. CrX_3 MLs consist of halide-Cr-halide triple layers, and Cr atoms are arranged in the honeycomb structure. The unit cell used in the first-principles calculations is shown by the red dashed quadrilateral. The calculated geometric parameters and magnetic properties are summarized in Table I and Table S1. It can be clearly seen that lattice parameter increases from $CrCl_3$, $CrBr_3$ to CrI_3, which is in accordance with previous reports [15,28,29]. The calculated band structure shows that the single-layer $CrCl_3$ is a FM insulator with an indirect band gap of 2.59 eV, as displayed in the Fig. S2(a) of the Supplemental Material [30].

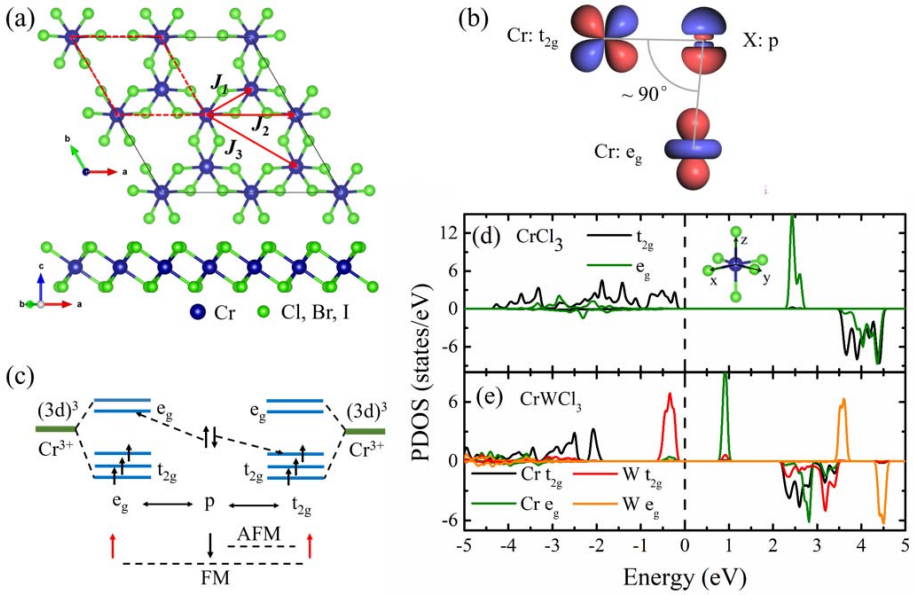

FIG. 1. (a) Top and side views of CrX_3 (X = Cl, Br, I) ML. The unit cell is indicated

by the red dashed quadrilateral. Blue and green balls represent Cr and X atoms, respectively. The first (J_1), second (J_2) and third (J_3) nearest neighboring exchange interaction parameters are indicated by red arrows. (b) and (c) Sketch of the FM superexchange interaction in $CrCl_3$ ML via the $t_{2g}-p-e_g$ orbitals. (d) The projected density of states (PDOS) of Cr 3d orbitals in $CrCl_3$ ML. (e) The PDOS of Cr and W 3d/5d orbitals in $CrWCl_6$ ML. Positive (negative) values refer to up (down) spins. Fermi level is set at zero energy. In (d) and (e) the atomic orbitals are projected onto the local coordinate frame, in which the *z* axis points along the $CrCl_6$ octahedra as shown in the inset of (d).

Now we investigate the magnetic anisotropy energy (E_{MAE}), a critical parameter to stabilize the long-range magnetic ordering against thermal fluctuations in 2D materials. In principle, the magnetic anisotropy is mainly contributed by two terms: (1) magnetocrystalline anisotropy (E_{MCA}) induced by the spin-orbit coupling (SOC), and (2) magnetic shape anisotropy (E_{MSA}) resulting from the dipole-dipole interaction, i.e., $E_{\mathrm{MAE}}=E_{\mathrm{MCA}}+E_{\mathrm{MSA}}$. Here, E_{MCA} is obtained by calculating the total energy change (with SOC included) as the magnetization rotates from the in-plane to the perpendicular directions with respect to the CrX_3 layer ($E_{\mathrm{MCA}}=E_{\square}^{\mathrm{SOC}}-E_{\perp}^{\mathrm{SOC}}$). On the other hand, E_{MSA} ($E_{\mathrm{MSA}}=E_{\square}^{\mathrm{Dipole}}-E_{\perp}^{\mathrm{Dipole}}$) is calculated according to the energy of magnetic dipole-dipole interactions as:

$$E^{\mathrm{Dipole}}=-\frac{1}{2}\frac{\mu_0}{4\pi r_{ij}^3}\sum_{i=1}^{N}\sum_{j=1}^{r_{\max}}\left[\vec{M}_1\cdot\vec{M}_2-\frac{3}{r_{ij}^2}\left(\vec{M}_1\cdot\vec{r_{ij}}\right)\left(\vec{M}_2\cdot\vec{r_{ij}}\right)\right]. \quad (1)$$

Here $\boldsymbol{M_i}$ represents the local magnetic moments and $\boldsymbol{r_{ij}}$ are vectors that connects the sites *i* and *j*. Since this energy converges very slowly with respect to the cutoff of r_{ij} [Fig. S2(b)], we expanded the range to $r_{\max}=1000$ Å to ensure the numerical reliability.

Table I. The calculated E_{MCA}, E_{MSA}, E_{MAE}, exchange interaction parameters and Curie temperatures of CrX_3, $CrWCl_6$ and $CrMoCl_6$ ML. The units of E_{MCA}, E_{MSA} and E_{MAE} are μeV per magnetic atom and those of J_1, J_2 and J_3 are meV. Experimental Curie temperatures are also listed for comparison.

Cases	E_{MCA}	E_{MSA}	E_{MAE}	J_1	J_2	J_3	T_C (K)	Exp. T_C (K)
$CrCl_3$	18	-58	-40	5.21	0.33	-0.08	17*	27 (bulk)[d]
$CrBr_3$	157	-47	110	4.66	0.70	-0.33	31	47 (bulk)[d]
CrI_3	655	-37	618	8.10	1.27	0.00	70	70 (bulk)[d], 45 (ML)[e]
$CrMoCl_6$	98	-49	49	5.80	0.18	-0.13	24	-
$CrWCl_6$	1113	-42	1071	14.83	0.12	-0.18	76	-

[d]Ref. [31]

[e]Ref. [8]

*For $CrCl_3$, we assumed an out-of-plane magnetization solely comes from the E_{MCA} term to get a finite value of T_C.

The calculated magnetic anisotropy energies of CrX_3 MLs are summarized in Table I. It is interesting that they all have positive E_{MCA}, as found in previous theoretical studies. This indicates that their magnetocrystalline anisotropy parts favor the perpendicular magnetization, even though the magnitude of E_{MCA} decreases monotonically as we move up from I, Br to Cl in the periodic table. Note that the monotonic decrease of E_{MCA} is mainly due to the SOC weakening from I, Br to Cl [32]. On the contrary, their shape anisotropy favors an in-plane alignment of magnetization and the magnitude E_{MSA} changes in a narrow range as the local magnetic moments are the same in the three MLs. As a result of the competition, the net magnetic anisotropy energy, E_{MAE}, is negative (in-plane easy axis) for $CrCl_3$ ML but is positive (perpendicular easy axis) for $CrBr_3$ or CrI_3 MLs, in perfect agreement with experiment. Obviously, E_{MSA} can be comparable to or even larger than E_{MCA}, especially when the SOC of chalcogenides is weak. This calls for attention on the consideration of the E_{MSA} for studies of 2D magnetic materials [33,34], which has been neglected in most works in this realm [14,15].

Another fundamental parameter for the determination of the Curie temperature of magnetic systems is the exchange interaction. To obtain the exchange parameters, J_i, we mapped the DFT total energies of several configurations onto the following classical Heisenberg Hamiltonian:

$$H = -J_1 \sum_{\langle ij \rangle} \overrightarrow{S_i} \cdot \overrightarrow{S_j} - J_2 \sum_{\langle\langle ij \rangle\rangle} \overrightarrow{S_i} \cdot \overrightarrow{S_j} - J_3 \sum_{\langle\langle\langle ij \rangle\rangle\rangle} \overrightarrow{S_i} \cdot \overrightarrow{S_j}, \quad (2)$$

where J_1, J_2 and J_3 represent the nearest, next nearest and third nearest neighbor exchange interactions, respectively [Fig. 1(a)]. For CrX_3 MLs, we designed four different magnetic configurations as shown in Fig. S3. As summarized in Table I, the nearest neighbor exchange interaction (J_1) is dominating for the establishment of the FM ground state. The next nearest neighbor interaction (J_2) prefers the FM ordering as well, but the weak third nearest neighbor interaction (J_3) tends to be antiferromagnetic (AFM). Note that the CrI_3 ML has the largest J_1 and J_2.

The FM J_1 originates from the competition between a strong FM superexchange via the near-90° Cr-X-Cr bonds and a weak Cr-Cr AFM direct exchange. Here we take $CrCl_3$ ML as an example. As shown in Figs. 1(c) and 1(d), the Cr-d orbitals split into three low-lying half-occupied t_{2g} and two high-lying empty e_g states. The Cr-Cl-Cr angle (95.5°) is close to 90° in the superexchange path [Fig. 1(b)] and thus gives rise to a FM superexchange interaction according to the Goodenough−Kanamori−Anderson rules [35-37] [Fig. 1(c)]. As the electronic configuration of Cr^{3+} ion is $t_{2g}^3 e_g^0$, the direct exchange between two nearest neighboring Cr^{3+} ions is AFM. However, the direct AFM exchange is weak because of the large distance (3.53 Å) between adjacent Cr ions. As a result, the FM superexchange overtakes the AFM direct exchange, resulting in a net FM J_1. As for J_2, it involves several possible Cr-Cl-Cl-Cr superexchange paths which contribute either

FM or AFM coupling, depending on the corresponding angles [15]. As a result of the competitions between multiple FM and AFM coupling mechanisms, J_2 is weak and FM.

B. Formation energy of $Cr_{8-x}W_xCl_{24}$ (x=0~8)

As a strong perpendicular anisotropy [38] is mostly required for 2D magnetic films, it is desirable to find ways to enhance the weak magnetic anisotropy of CrX_3 MLs. We perceive that substituting Cr by isovalent W atoms might be a good approach, since W has the same electronic configuration as Cr but much larger SOC. Therefore, we may expect a larger perpendicular magnetic anisotropy and thereby a higher T_C. To demonstrate this concept, we used $CrCl_3$ ML as our modeling system. At first, we need to investigate whether Cr and W atoms can be intermixed. We considered 9 different W concentrations by constructing a 2×2 supercell $Cr_{8-x}W_xCl_{24}$ with $x=0\sim8$. For each W concentration, there are a large number of possible substitution configurations. In order to find out the optimal distribution patterns of Cr and W atoms, we considered all possible distributions of Cr and W in the 2×2 supercell. The detailed structure configurations for different W concentration (x) in the alloyed systems are given in the Supplemental Material (Fig. S1). For each ground state of $Cr_{8-x}W_xCl_{24}$ (see Supplemental Material), the formation energy $\Delta E_f\left(Cr_{8-x}W_xCl_{24}\right)$ is obtained from:

$$\Delta E_f\left(Cr_{8-x}W_xCl_{24}\right)=E\left(Cr_{8-x}W_xCl_{24}\right)-(8-x)E\left(CrCl_3\right)-xE\left(WCl_3\right). \quad (3)$$

The calculated formation energy as a function of W concentration (x) is shown in Fig. 2(a). We see that the relative energies of the mixed phases are lower by ~0.031 eV per magnetic atom compared to those of the pure phases, namely, $CrCl_3$ and WCl_3 MLs. This indicates that the mixed phases can stably exist without phase separation.

To further examine the feasibility of making the (Cr, W) mixed phases in experiments, we calculated the formation enthalpy $\Delta H_f\left(Cr_{8-x}W_xCl_{24}\right)$ by varying chemical potentials of Cr, W and Cl as:

$$\Delta H_f\left(Cr_{8-x}W_xCl_{24}\right)=E\left(Cr_{8-x}W_xCl_{24}\right)-kT\ln C_8^x-(8-x)\mu_{Cr}-x\mu_W-24\mu_{Cl}. \quad (4)$$

In Eq. (4), $E\left(Cr_{8-x}W_xCl_{24}\right)$ is the ground state energy of the mixed phase. The second term is the configuration entropy (T = 875 K is used here). μ_{Cr}, μ_W and μ_{Cl} represent the chemical potentials of Cr, W and Cl relative to the chemical potentials of their elemental phases. Here, we assume that the source of Cl atoms is the same for different W concentrations, so the term, $-24\mu_{Cl}$, in the Eq. (4) is a constant.

Fig. 2(b) gives the lowest ΔH_f of $Cr_{8-x}W_xCl_{24}$ in the (μ_{Cr}, μ_W) plane within ranges of $-2.48\,\text{eV}<\mu_{Cr}<0$ and $-6.54\,\text{eV}<\mu_W<0$. One may see that the mixed states can survive in $x=1\sim7$, which means that mixing of W into $CrCl_3$ ML is

feasible in the W-rich condition around $\mu_W = -2.5 \sim -5$ eV. The stable region in this phase diagram has no obvious changes except that the olive area got bigger with decreasing the value of U in DFT calculations (see Fig. S4 in Supplemental Material), and the evenly mixed $Cr_4W_4Cl_{24}$ with x = 4 (i.e. $CrWCl_6$) appears to be the most preferential configuration for all cases.

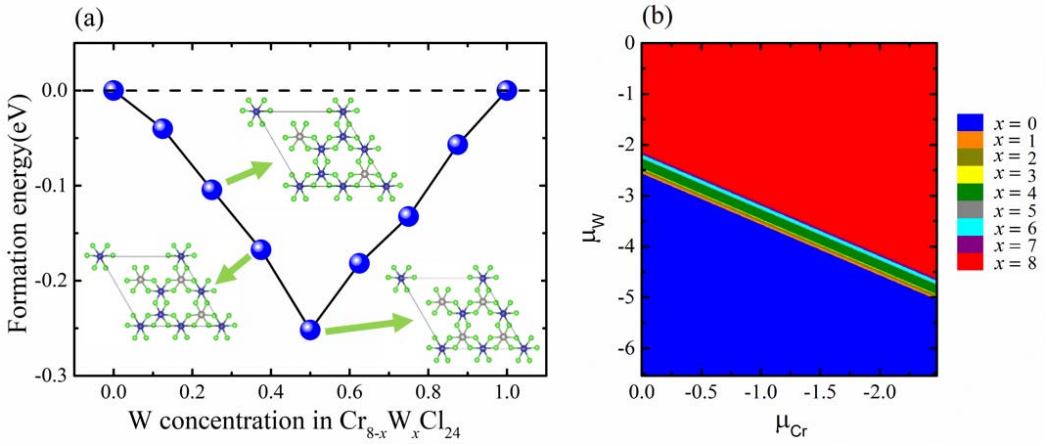

FIG. 2. (a) Formation energy $\Delta E_f\left(Cr_{8-x}W_xCl_{24}\right)$ as a function of W concentration in $Cr_{8-x}W_xCl_{24}$. Insets show the lowest-energy configurations for $x = 2 \sim 4$. (b) The phase diagram of the stable region of $Cr_{8-x}W_xCl_{24}$ (x = 0~8) with different W concentrations. The number of W atoms in $Cr_{8-x}W_xCl_{24}$ ML is labeled by x. The right (bottom) and left (top) boundaries of chromium (tungsten) chemical potential correspond to the so-called Cr (W)-rich (Cr or W bulk as the reservoir) and Cr (W)-poor (Cr or W atom as the reservoir) conditions, respectively.

As the Cr and W atoms tend to be distributed rather uniformly, the unit cell can be reduced back to $CrWCl_6$ ML, which makes the discussion and comparison rather straightforward. Because of the strong SOC of W, E_{MCA} of the $CrWCl_6$ ML has a large positive value, 1114 μeV per magnetic atom. As the value of E_{MSA} is almost unchanged from that of the Cr_2Cl_6 ML, the magnetic easy axis of $CrWCl_6$ ML is stably perpendicular as desired, with a giant MAE of 1071 μeV per magnetic atom (Table I). This value is even comparable with MAEs of many FM transition metal thin films such as Fe, Co, and Ni on different substrates [39].

C. Origin of the enhanced MCA in $CrWCl_6$

To investigate the physical origin of the giant perpendicular E_{MCA} of $CrWCl_6$ ML, we plotted its band structure in Fig. 3(a). After W atoms are introduced, the band gap is 1.07 eV, with the unoccupied spin up states of the Cr_2Cl_6 ML moving toward the Fermi level. However, we can't draw a simple conclusion for the large E_{MCA} solely from the reduced band gap. Here, we analyze the tendency of E_{MCA} of the $CrWCl_6$ ML with respect to the shift of the Fermi level, using the torque method and rigid band model [40,41]. Note that the E_{MCA} obtained from the toque method, 1089 μeV per magnetic atom is very close to that listed in Table I (1114 μeV), indicating the

reliability of the torque method for these systems. We decompose E_{MCA} into contributions from different atoms or spin channels and show the results in Fig. 3(b) and Fig. S5(b). Although the E_{MCA} in CrI_3 MLs arises predominately from the SOC of the ligand iodine atoms [31], it can be seen that in $CrWCl_6$ ML W atoms contribute the most to E_{MCA}, i.e., 990 μeV per magnetic atom. The same conclusion can also be drawn by selectively scaling the SOC strength of each element as shown in Figs. S6(a) and S6(b). From the spin resolutions, we find that the dominating part is $\Delta E^{\uparrow\downarrow/\downarrow\uparrow}$ [Fig. S5(b)], which contributes 60% of E_{MCA}. If we move the Fermi energy down by 0.5 eV, $\Delta E^{\uparrow\downarrow/\downarrow\uparrow}$ exhibits a sudden change as shown in Fig. S5(b), indicating that electronic states near -0.5 eV play the main role in producing the large positive E_{MCA} of the $CrWCl_6$ ML. By projecting wave functions of states around this energy to the W site [Fig. 3(a)], we reach a conclusion that the perpendicular E_{MCA} mainly results from the SOC interactions between the occupied spin-up $d_{xz/yz}$ [bands -1, -3 in Fig. 3(a)] and unoccupied spin-down d_{z^2} states [band 1 in Fig. 3(a)] of W through the L_x operator. As W has a large SOC strength, this coupling produces a large perpendicular E_{MCA}. Note that due to the requirement of the second-order perturbation formula (see Part IV in Supplemental Material), the atomic orbitals are projected onto the global coordinate frame, in which the z axis points along the out-of-plane easy axis. This is different from the local coordinate frame (see the inset in Fig. 1(d)) used in Figs. 1(d) and 1(e).

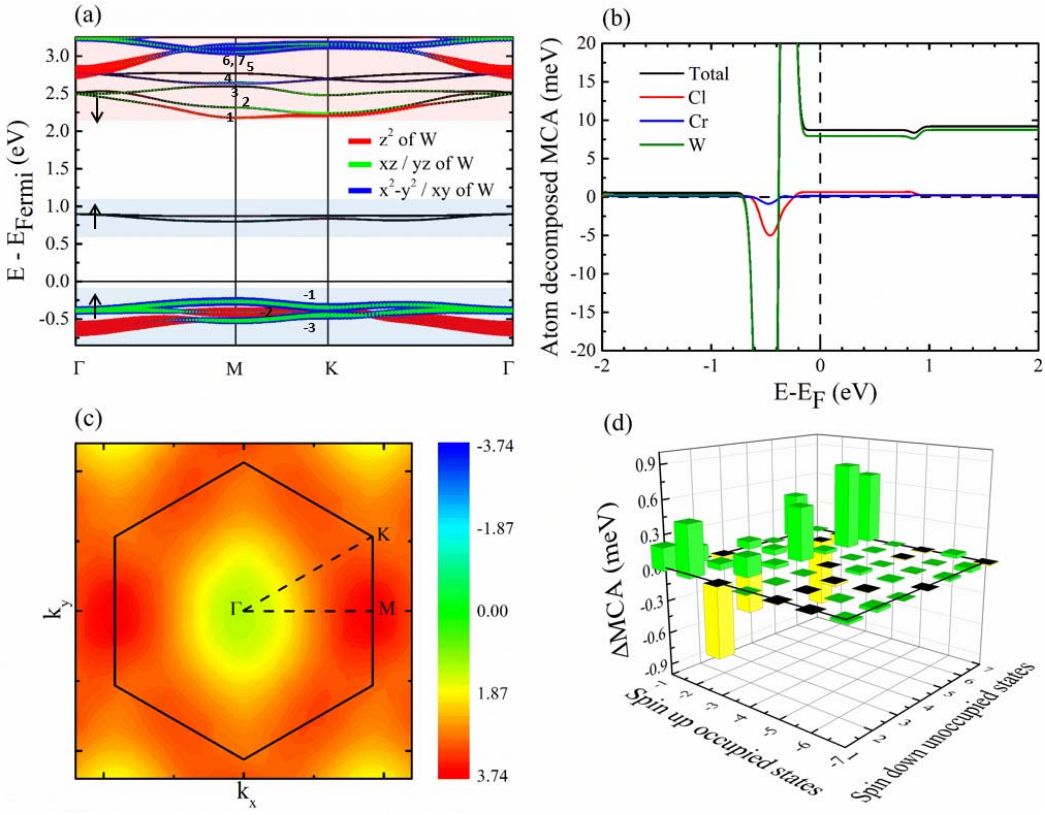

FIG. 3. (a) Orbital resolved band structure of $CrWCl_6$ ML. The |m| = 0, 1, 2 orbitals of W are represented by red, green, blue lines, respectively, and the line width scales with their weights. Band indices are marked by numbers. The up and down spin

states are indicated by the light blue and red shades, respectively. (b) The decomposition of the total E_{MCA} to the contributions of different atoms in $CrWCl_6$ ML. The black line shows the total E_{MCA}, and the red, blue and olive lines represent the contributions from Cl, Cr and W atoms, respectively. (c) Distribution of ΔE_{MCA} in the BZ. The blue and red colors represent negative and positive contributions, respectively. (d) Contributions of each pair of spin-up occupied states and spin-down unoccupied states for summation over all the K and M points in the first BZ.

We note that the nearest neighbor exchange coupling parameter, J_1, is also large for $CrWCl_6$ ML, up to14.8 meV (Table I), due to the stronger W-Cl hybridization. The energy separations between the occupied W-t_{2g} orbitals and empty Cr-e_g orbitals in $CrWCl_6$ are largely reduced compared to their counterparts in $CrCl_3$ [42] [Figs. 1(d) and 1(e)]. Since the FM superexchange arises from the virtual exchange between $t_{2g}-p-e_g$ orbitals, this reduction in energy separation enhances the FM superexchange interaction, and thus leads to a larger J_1.

Interestingly, the perpendicular magnetic anisotropy of $CrWCl_6$ ML can be further enhanced by strains. For example, an in-plane tensile strain of 5% may increase E_{MCA} of the $CrWCl_6$ ML to 2375 μeV per magnetic atom, more than twice as large as the unstrained one. By decomposing $\Delta E_{MCA}=E_{MCA}^{strained}-E_{MCA}^{unstrained}$ to the contributions of different **k**-points in the first Brillouin zone (BZ) [Fig. 3(c)], we found that ΔE_{MCA} mainly occurs around the M point. We further resolve the ΔE_{MCA} to contributions of different pairs of occupied-unoccupied states according to the second-order perturbation formula (see Part IV in Supplemental Material). The results are shown in Fig. 3(d), where the band indices are given according to Fig. 3(a). Clearly, the eye-catching pairs are (-1, 2), (-3, 4) and (-3, 7). Fig. S5 gives more details about their energy separation and matrix elements.

D. The enhanced Curie temperature of $CrWCl_6$

Finally, we determined the T_C of $CrWCl_6$ using the renormalized spin-wave theory (RSWT) [43,44] to show the benefit of Cr-W intermixing. It is recognized that the linear spin-wave theory (LSWT) typically overestimates T_C of 2D magnetic films [43,44], and the inclusion of multi-magnon scattering (i.e., the non-linear corrections in [32]) is essential to get reliable estimation of their T_C. Through the studies of magnetic field dependence of T_C in few-layer and bulk $Cr_2Ge_2Te_6$, it was shown that the RSWT method can reach quantitative agreement with experiments [7]. Here, we outline the essence of the RSWT. In LSWT, through the Holstein-Primakoff transformation, the spin operator $\mathbf{S}_{\mathbf{l}v}=\left(S_{\mathbf{l}v}^x,S_{\mathbf{l}v}^y,S_{\mathbf{l}v}^z\right)$ on site v in the **l**-th unit cell in Eq. (2) is rewritten by the deviation creation and annihilation operators $a_{\mathbf{l}v}^+$ and $a_{\mathbf{l}v}$, i.e., $S_{\mathbf{l}v}^+\approx\sqrt{2S}a_{\mathbf{l}v}$, $S_{\mathbf{l}v}^-\approx\sqrt{2S}a_{\mathbf{l}v}^+$, and $S_{\mathbf{l}v}^z\approx S-a_{\mathbf{l}v}^+a_{\mathbf{l}v}$. In the RSWT, however, $\mathbf{S}_{\mathbf{l}v}$ is expanded up to second order terms of $a_{\mathbf{l}v}^+$ and $a_{\mathbf{l}v}$ to take into account the magnon-magnon interaction at finite temperatures [44]. In this case, the operator $S_{\mathbf{l}v}^z$ is the same as that in LSWT but spin ladder operators $S_{\mathbf{l}v}^+$ and $S_{\mathbf{l}v}^-$ are in the form of

$$S_{\mathbf{l}v}^{+} \approx \sqrt{2S}\left(a_{\mathbf{l}v} - a_{\mathbf{l}v}^{+}a_{\mathbf{l}v}a_{\mathbf{l}v}/4S\right), \tag{5}$$

$$S_{\mathbf{l}v}^{-} \approx \sqrt{2S}\left(a_{\mathbf{l}v}{}^{+} - a_{\mathbf{l}v}^{+}a_{\mathbf{l}v}^{+}a_{\mathbf{l}v}/4S\right). \tag{6}$$

Using Eq. (5-6) and the Fourier transformation $a_{\mathbf{l}v}^{+} = \frac{1}{\sqrt{N}}\sum_{\mathbf{k}} e^{-i\mathbf{k}\cdot\mathbf{b}} b_{\mathbf{b}v}^{+}$ and $a_{\mathbf{l}v} = \frac{1}{\sqrt{N}}\sum_{\mathbf{k}} e^{i\mathbf{k}\cdot\mathbf{b}} b_{\mathbf{b}v}$, we transform the spin Hamiltonian Eq. (2) from the real space to the reciprocal space and the resulting Hamiltonian contains the magnon-magnon interaction [44]. Following the Bose-Einstein statistics, the total magnetization $M(T)$ as a function of temperature T is expressed as:

$$\frac{M(T)}{M_0} = 1 - \frac{1}{nNS}\sum_{\pm}\sum_{\mathbf{k}}\left[\exp\left(\frac{\hbar\omega_{\mathbf{k}\pm}}{k_B T}\right) - 1\right]^{-1} \tag{7}$$

where N and n are the numbers of unit cells and magnetic basis atoms in each unit cell, respectively. M_0 denotes the fully polarized magnetization at T = 0 K. "±" represents the two magnon braches, i.e., the in-phase acoustic mode and the anti-phase optical mode. $\omega_{\mathbf{k}\pm}$ is the magnon spectrum solved from Eq. (6). The Curie temperature, T_C, is determined by the temperature at which the total magnetization becomes zero, i.e. $M(T) = 0$.

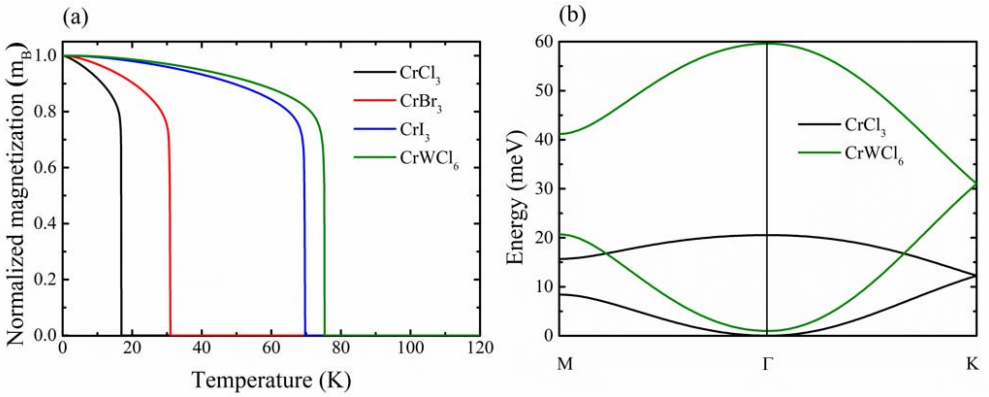

FIG. 4. (a) The renormalized magnetization $\frac{M(T)}{M_0}$ as a function of temperature T. T_C is determined by the temperature at $M(T) = 0$. (b) Spin-wave excitation (magnon) spectrums of $CrCl_3$ ML and $CrWCl_6$ ML.

The calculated total magnetizations of $CrCl_3$, $CrBr_3$, CrI_3 and $CrWCl_6$ MLs by RSWT as a function of temperature are shown in Fig. 4(a), and their values of T_C are listed in Table I. It should be pointed out that, in principle, $CrCl_3$ ML cannot sustain a long-range magnetic order since its magnetic easy axis is in-plane, as mentioned previously. For a better comparison, we ignore the E_{MSA} term for the $CrCl_3$ ML and

assume an out-of-plane magnetization that solely comes from E_{MCA}. Nevertheless, this hypothetical $CrCl_3$ ML still has a low T_C, only 17 K. By mixing with W, the T_C of $CrWCl_6$ ML can be as high as 76 K, even higher than that of CrI_3 ML. From the spin wave (magnon) spectrum as shown in Fig. 4(b), we see that the optical branch of $CrWCl_6$ ML shifts to a much higher energy compared with that of $CrCl_3$ ML, indicating the difficulty to excite it and hence the T_C is significantly improved.

We also examined if Mo has a similar effect as W. As summarized in Table I and Fig. S7(b), we found that both MCA and Curie temperature are enhanced from pristine $CrCl_3$, with E_{MCA} = 98 μeV per magnetic atom and T_C = 24 K. These values are, however, much smaller than those cause by W substitution. This is understandable sine the SOC strength of Mo is smaller than W. Furthermore, as shown in Fig. S6(a), the energy separations between the occupied Mo-t_{2g} orbitals and empty Cr-e_g orbitals in $CrMoCl_6$ are smaller than that of in $CrWCl_6$ [Fig. 1(e)], indicating a weaker virtual exchange between $t_{2g}-p-e_g$ orbitals, and thereby a lower T_C. We may thus conclude that W substitution is better than Mo for practical purposes.

IV. SUMMARY

In conclusion, we systematically investigated the 2D ferromagnetism of $CrCl_3$ and $Cr_{8-x}W_xCl_{24}$ (x = 0~8) MLs. We unveil that the magnetic shape anisotropy, which has been neglected in most of previous works, is responsible for the observed in-plane magnetic easy axis of $CrCl_3$ monolayer. This indicates that it is vital to consider E_{MSA} for studies of weak magnetic anisotropy thin films. Furthermore, this in-plane ferromagnetism can be tuned to the desirable perpendicular one by substituting some Cr atoms with isovalent W atoms. The theoretical feasibility and experimental maneuverability of the intermixed $Cr_{8-x}W_xCl_{24}$ MLs were thoroughly studied. We find that the intermediate concentration doping with x = 4~6 is energetically preferred and thereby can be easily synthesized under the W-rich condition around $\mu_W = -2.5 \sim -5$ eV in experiments. In particular, the $CrWCl_6$ ML has a significantly enhanced perpendicular magnetic anisotropy, a large exchange interaction, and hence a high Curie temperature up to 76 K according to our RSWT simulations. Our work gives insights into understanding the two-dimensional ferromagnetism of van der Waals magnetic MLs and suggests a route toward improving the performance of CrX_3 MLs for spintronic applications.

ACKNOWLEDGMENTS

Work was supported by DOE-BES (Grant No. DE-FG02-05ER46237). Computer simulations were partially performed at the U.S. Department of Energy Supercomputer Facility (NERSC). F.X and Z.W. acknowledge support by the Basic Research Program of China under Grant No. 2015CB921400.

References

[1] K. S. Novoselov, A. K. Geim, S. V. Morozov, D. Jiang, Y. Zhang, S. V. Dubonos, I. V. Grigorieva, and A. A. Firsov, Science **306**, 666 (2004).

[2] C. R. Dean, A. F. Young, I. Meric, C. Lee, L. Wang, S. Sorgenfrei, K. Watanabe, T. Taniguchi, P. Kim, K. L. Shepard, and J. Hone, Nat. Nanotechnol. **5**, 722 (2010).

[3] S. Cahangirov, M. Topsakal, E. Aktürk, H. Şahin, and S. Ciraci, Phys. Rev. Lett. **102**, 236804 (2009).

[4] K. F. Mak, C. Lee, J. Hone, J. Shan, and T. F. Heinz, Phys. Rev. Lett. **105**, 136805 (2010).

[5] Q. H. Wang, K. Kalantar-Zadeh, A. Kis, J. N. Coleman, and M. S. Strano, Nat. Nanotechnol. **7**, 699 (2012).

[6] H. Liu, A. T. Neal, Z. Zhu, Z. Luo, X. Xu, D. Tománek, and P. D. Ye, ACS Nano **8**, 4033 (2014).

[7] C. Gong, L. Li, Z. Li, H. Ji, A. Stern, Y. Xia, T. Cao, W. Bao, C. Wang, Y. Wang, Z. Q. Qiu, R. J. Cava, S. G. Louie, J. Xia, and X. Zhang, Nature **546**, 265 (2017).

[8] B. Huang, G. Clark, E. Navarro-Moratalla, D. R. Klein, R. Cheng, K. L. Seyler, D. Zhong, E. Schmidgall, M. A. McGuire, D. H. Cobden, W. Yao, D. Xiao, P. Jarillo-Herrero, and X. Xu, Nature **546**, 270 (2017).

[9] B. Shabbir, M. Nadeem, Z. Dai, M. S. Fuhrer, Q.-K. Xue, X. Wang, and Q. Bao, Appl. Phys. Rev. **5**, 041105 (2018).

[10] M. Gibertini, M. Koperski, A. F. Morpurgo, and K. S. Novoselov, Nat. Nanotechnol. **14**, 408 (2019).

[11] C. Gong and X. Zhang, Science **363**, eaav4450 (2019).

[12] K. S. Burch, D. Mandrus, and J.-G. Park, Nature **563**, 47 (2018).

[13] N. D. Mermin and H. Wagner, Phys. Rev. Lett. **17**, 1133 (1966).

[14] L. Webster and J.-A. Yan, Phys. Rev. B **98**, 144411 (2018).

[15] W.-B. Zhang, Q. Qu, P. Zhu, and C.-H. Lam, J. Mater. Chem. C **3**, 12457 (2015).

[16] M. Abramchuk, S. Jaszewski, K. R. Metz, G. B. Osterhoudt, Y. Wang, K. S. Burch, and F. Tafti, Adv. Mater. **30**, 1801325 (2018).

[17] X. Cai, T. Song, N. P. Wilson, G. Clark, M. He, X. Zhang, T. Taniguchi, K. Watanabe, W. Yao, D. Xiao, M. A. McGuire, D. H. Cobden, and X. Xu, Nano Lett. **19**, 3993 (2019).

[18] H. H. Kim, B. Yang, S. Li, S. Jiang, C. Jin, Z. Tao, G. Nichols, F. Sfigakis, S. Zhong, C. Li, S. Tian, D. G. Cory, G.-X. Miao, J. Shan, K. F. Mak, H. Lei, K. Sun, L. Zhao, and A. W. Tsen, Proc. Natl. Acad. Sci. U.S.A. **116**, 11131 (2019).

[19] M. A. McGuire, G. Clark, S. Kc, W. M. Chance, G. E. Jellison, V. R. Cooper, X. Xu, and B. C. Sales, Physical Review Materials **1**, 014001 (2017).

[20] K. L. Seyler, D. Zhong, D. R. Klein, S. Gao, X. Zhang, B. Huang, E. Navarro-Moratalla, L. Yang, D. H. Cobden, M. A. McGuire, W. Yao, D. Xiao, P. Jarillo-Herrero, and X. Xu, Nature Physics **14**, 277 (2018).

[21] Z. Zhang, J. Shang, C. Jiang, A. Rasmita, W. Gao, and T. Yu, Nano Lett. **19**, 3138 (2019).

[22] Y. Hou, J. Kim, and R. Wu, Sci. Adv. **5**, eaaw1874 (2019).

[23] P. E. Blöchl, Phys. Rev. B **50**, 17953 (1994).

[24] G. Kresse and D. Joubert, Phys. Rev. B **59**, 1758 (1999).

[25] G. Kresse and J. Furthmüller, Phys. Rev. B **54**, 11169 (1996).

[26] G. Kresse and J. Furthmüller, Computational Materials Science **6**, 15 (1996).

[27] J. P. Perdew, K. Burke, and M. Ernzerhof, Phys. Rev. Lett. **77**, 3865 (1996).

[28] J. Liu, Q. Sun, Y. Kawazoe, and P. Jena, Phys. Chem. Chem. Phys. **18**, 8777 (2016).

[29] S. Tomar, B. Ghosh, S. Mardanya, P. Rastogi, B. S. Bhadoria, Y. S. Chauhan, A. Agarwal, and S. Bhowmick, J. Magn. Magn. Mater. **489**, 165384 (2019).

[30] See Supplemental Material for more details on the structure and magnetic calculations, such as formation energies with different Hubbard U, the second-order perturbation theory used to explain the MCA, decomposition of the MCA and effects of Mo substitution and Ref. [31], Ref [45] and Ref. [46s].

[31] M. A. McGuire, H. Dixit, V. R. Cooper, and B. C. Sales, Chem. Mater. **27**, 612 (2015).

[32] J. L. Lado and J. Fernández-Rossier, 2D Mater. **4**, 035002 (2017).

[33] Y. Fang, S. Wu, Z.-Z. Zhu, and G.-Y. Guo, Phys. Rev. B **98**, 125416 (2018).

[34] V. Kumar Gudelli and G.-Y. Guo, New J. Phys. **21**, 053012 (2019).
[35] J. B. Goodenough, Phys. Rev. **100**, 564 (1955).
[36] J. Kanamori, J. Phys. Chem. Solids **10**, 87 (1959).
[37] P. W. Anderson, Phys. Rev. **79**, 350 (1950).
[38] S. M. Thompson, J. Phys. D: Appl. Phys. **41**, 093001 (2008).
[39] R. Wu and A. J. Freeman, J. Magn. Magn. Mater. **200**, 498 (1999).
[40] X. Wang, R. Wu, D. Wang, and A. J. Freeman, Phys. Rev. B **54**, 61 (1996).
[41] J. Hu and R. Wu, Phys. Rev. Lett. **110**, 097202 (2013).
[42] C. Huang, J. Feng, F. Wu, D. Ahmed, B. Huang, H. Xiang, K. Deng, and E. Kan, J. Am. Chem. Soc. **140**, 11519 (2018).
[43] M. Bloch, Phys. Rev. Lett. **9**, 286 (1962).
[44] Z. Li, T. Cao, and S. G. Louie, J. Magn. Magn. Mater. **463**, 28 (2018).
[45] B. Morosin and A. Narath, J. Chem. Phys. **40**, 1958 (1964).
[46] L. Handy and N. W. Gregory, J. Am. Chem. Soc. **74**, 891 (1952).